JACS
JOURNAL OF THE AMERICAN CHEMICAL SOCIETY
pubs.acs.org/JACS
Article

Adaptive Ion Channels Formed in Ultrathin and Semicrystalline Polymer Interphases for Stable Aqueous Batteries

Pengyu Chen,[§] Shuo Jin,[§] Shifeng Hong, Yufeng Qiu, Zheyuan Zhang, Yuanze Xu, Yong Lak Joo, Lynden A. Archer,* and Rong Yang*

Cite This: *J. Am. Chem. Soc.* 2024, 146, 3136–3146

ABSTRACT: Aqueous Zn batteries have recently emerged as promising candidates for large-scale energy storage, driven by the need for a safe and cost-effective technology with sufficient energy density and readily accessible electrode materials. However, the energy density and cycle life of Zn batteries have been limited by inherent chemical, morphological, and mechanical instabilities at the electrode−electrolyte interface where uncontrolled reactions occur. To suppress the uncontrolled reactions, we designed a crystalline polymer interphase for both electrodes, which simultaneously promotes electrode reversibility via fast and selective Zn transport through the adaptive formation of ion channels. The interphase comprises an ultrathin layer of crystalline poly(1*H*,1*H*,2*H*,2*H*-perfluorodecyl acrylate), synthesized and applied as a conformal coating in a single step using initiated chemical vapor deposition (iCVD). Crystallinity is optimized to improve interphase stability and Zn-ion transport. The optimized interphase enables a cycle life of 9500 for Zn symmetric cells and over 11,000 for Zn-MnO_2 full-cell batteries. We further demonstrate the generalizability of this interphase design using Cu and Li as examples, improving their stability and achieving reversible cycling in both. The iCVD method and molecular design unlock the potential of highly reversible and cost-effective aqueous batteries using earth-abundant Zn anode materials, pointing to grid-scale energy storage.

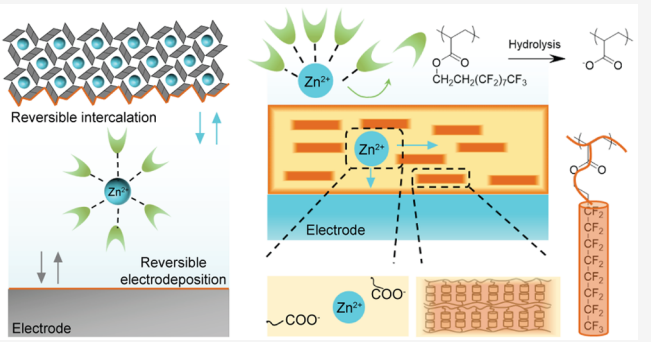

INTRODUCTION

Reliable, safe, and cost-effective energy storage technologies are key to sustaining the current way of life in an "electrify-everything" strategy for lowering humanity's carbon footprint.[1,2] Aqueous zinc(Zn) ion batteries, such as a Zn−MnO_2 battery, are considered among the most promising technologies for beyond-lithium, stationary storage for the electric grid.[3] Such batteries are also of interest in some portable applications, including flexible devices and robotics[4,5] due to their high operating voltage (~1.6 V),[6] high charging/discharging rate,[7] cost-effectiveness,[8] and safety.[9] Nevertheless, existing aqueous zinc-ion batteries are fundamentally limited by inherent chemical, morphological, and mechanical instabilities at the electrode−electrolyte interface. Most failure modalities, including short-cutting, water decomposition/hydrogen evolution, self-discharge, and loss of cathodic active materials, have their causes rooted in uncontrolled reactions and byproducts that these reactions produce at electrode−electrolyte interfaces. As a result, the broad deployment of aqueous Zn-ion batteries has been hindered by the long-standing issues of a short cycle life and low energy efficiency. Interphases that mitigate the range of instabilities will extend the cycle life and unlock the potential of these low-cost aqueous batteries based on earth-abundant Zn anode materials.

The interfacial instabilities fundamentally stem from a convoluted interplay between physical and chemical processes; e.g., interfacial heterogeneity leads to uneven mass transport, which in turn promotes the irreversible capacity loss and conversion of active materials into a passivation layer, which exacerbates the interfacial heterogeneity (Figure S1).[2] On the anode side, Zn metal is subject to thermodynamic instability and electrochemical corrosion by water molecules,[10] giving rise to the deposition of solid byproducts (predominantly ZnO) on the anode. The solid layer introduces a high electrical resistance and chemical heterogeneity, thus fueling the nonuniform electrodeposition that unravels the battery performance.[10] Hydrogen evolution reaction (HER) also occurs at the Zn anode, creating gaseous byproducts and

Received: September 26, 2023
Revised: January 2, 2024
Accepted: January 3, 2024
Published: January 26, 2024

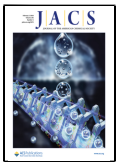

subsequent bulging, warping, and bloating of the battery. On the cathode side, here exemplified by MnO_2, the dissolution of Mn^{2+} into the aqueous electrolyte leads to capacity loss and irreversible crystallographic transformation of the cathodic material.[11] Constituents of the aqueous electrolyte, e.g., Zn^{2+}, SO_4^{2-}, and H_2O, further destabilize the cathode, promote the irreversible conversion of MnO_2 (under low potential), and form insoluble flakes of $ZnSO_4[Zn(OH)_2]_3{\cdot}xH_2O$ on the cathode, which cause significant loss of capacity.[12] Side reactions are also prevalent in Zn−I_2 and Zn−V_2O_5 batteries, rendering the interfacial instability a universal bottleneck for aqueous batteries.[6,13]

While prior research has performed substantial system-specific optimizations on the electrolyte,[14−16] the advances often add weight, new materials, and complexity to the cells compromising the cost-effectiveness or even performance of the battery.[17,18] As such, interphase design has emerged in recent years as a promising solution to the bottleneck issue of interfacial instability. Discrete interfacial material phases (interphases), formed intentionally at the electrodes for instance, are known to offer multiple degrees of freedom for regulating the kinetics and reversibility of electrochemical transformations inside a battery cell. Specifically for aqueous batteries, an ideal interphase should be water-resistant yet conductive to Zn cations; should form conformal coverage over the electrodes with few pinholes and other defects; and should be stable, both mechanically and electrochemically, in order to protect the electrodes from side reactions during extended cycles of charge and discharge.[19,20] Guided by these design principles, a plethora of synthesis techniques and interphase material chemistries have been reported, e.g., zwitterionic interphases,[21] metal−organic frameworks infused by hydrophobic liquids,[19] interdigitated indium hydroxide sulfate/Zn coating,[22] etc. While most previous research has focused on the flat Zn anode and improving the anodic stability by preparing artificial interphases, it is known that active material loss at the cathode in an aqueous electrolyte and parasitic reactions when these materials crossover to the anode are a failure mechanism of significant practical importance. We hypothesize that a stable aqueous Zn battery requires stable and conformal interphases at both electrodes. However, the development of cathodic interphases has been limited by the inability of the conventional coating techniques (such as spray coating,[23] dip coating, or spin coating[24]) to form conformal and uniform coverage on porous structures, such as those in a composite cathode (made of particles and binders). Surface tension effects are unavoidable in solution-based processing techniques, leading to dewetting of the coating from the substrate to form coating defects and bridging of narrow apertures. Consequently, there is a dearth of knowledge on the effects of purpose-built artificial interphases on cathode interfacial stability.

To create well-defined conformal interphases on the anode and cathode of a Zn battery simultaneously, we leverage an all-dry polymerization technique, namely, initiated chemical vapor deposition (iCVD).[25] During iCVD, monomers are vaporized and physisorbed on the substrate surface; they form a conformal polymer thin film through free-radical polymerization. The physisorption-based coating formation ensures that the iCVD coating technique is substrate-independent, enabling the application of an identical interphase chemistry on the anode and cathode to systematically understand its effects in aqueous batteries. Benefiting from the nonline-of-sight mass transfer as a result of the Knudsen diffusion under vacuum, iCVD has been used to create conformal polymer thin films over nanometer-scale structures with an aspect ratio as high as 600,[26] exceeding that of composite cathodes. The iCVD technique affords precise control over the coating thickness with nanoscale precision, enabling ultrathin films that are as thin as 10 nm to reduce the loss of conductivity.[27] Meanwhile, recent breakthroughs in achieving roll-to-roll manufacturing using iCVD supported the potential of the vacuum processes to be scaled up for electrode manufacturing, where conformal and uniform coatings were obtained on flexible substrates as large as 20 m^2.

As a demonstration, we used iCVD to create a series of hydrophobic polymer coatings using (1*H*,1*H*,2*H*,2*H*-perfluorodecyl acrylate) (PFDA) as the monomer. The synthesis was performed simultaneously on a MnO_2 cathode and a Zn metal anode. The choice of PFDA is informed by ample evidence that a fluorine-rich interphase suppresses side reactions between water and electrodes and other active materials.[6,28] Additionally, the secondary fluorinated species (e.g., ZnF_2) have been shown to promote lateral ion migration and facilitate a uniform ion flux at the Zn anode.[9] Meanwhile, pPFDA exhibits a controllable crystallization to balance the electrode protection and ionic conduction. The spontaneous hydrolysis of amorphous pPFDA at the interface creates a carboxylic acid group that works as adaptive ion channels to facilitate the cation migration, enhancing interfacial stability. We believe that this design of adaptive interphases is generalizable to other aqueous battery systems, where a conformal and ion-conductive coating on the anode and cathode protects the active materials and extends the cycle life of aqueous batteries.

MATERIALS AND METHODS

Materials. $ZnSO_4{\cdot}7H_2O$, $CuSO_4{\cdot}5H_2O$, $MnSO_4{\cdot}H_2O$, mPEG, PEG400, and LiTFSI were from Sigma-Aldrich. 0.25 mm Zn foil (99.994%), 0.254 mm Cu foil (99.9%), and 0.7 mm Li foil (99.99%) were bought from Alfa Aesar. Carbon clothes were purchased from Fuel Cell Store. Chemicals were used as is without any modifications. Deionized (DI) water was obtained from the Milli-Q water purification system. The resistivity of deionized water is 18.2 MΩ cm^{-1} at room temperature. Free-standing interwoven carbon fibers (Plain carbon cloth 1071 HCB) were purchased from Fuel Cell Store.

Initiated Chemical Vapor Deposition (iCVD). All the polymer coatings were created using iCVD technology in a custom-built cylindrical vacuum reactor (Sharon Vacuum Co Inc., Brockton, MA, USA). Thermal excitation of the initiators was provided by heating a 0.5 mm nickel/chromium filament (80% Ni/20% Cr, Goodfellow) mounted as a parallel filament array. Filament temperature was controlled by a feedback loop, whose reading came from a thermocouple attached to one of the filaments. The power feed is around 40 W, which gave a filament temperature of 300 °C. The filament holder straddled the deposition stage that was kept at desired substrate temperatures using a chiller. The vertical distance between the filament array and the stage was around 2 cm. Depositions were performed on three kinds of substrates: Si wafers (P/Boron <100>, Purewafer, San Jose, CA, USA), polished zinc foils, and the MnO_2 composite cathode on carbon cloth. The substrate was cooled by a circulator set as 20, delivering a substrate temperature of around 25 °C monitored by a thermal couple. Initiator, TBPO, and monomer, PFDA were used without further purification. During the iCVD depositions, TBPO was fed to the reactor at room temperature through a mass flow controller at 0.6 sccm. PFDA was heated to 80 °C in glass jars to create sufficient pressure to drive the vapor flow. The flow rate was designed at 0.15 sccm. The total pressure of the chamber was controlled by a butterfly valve at 500 mTorr. In situ

https://doi.org/10.1021/jacs.3c10638
J. Am. Chem. Soc. 2024, 146, 3136−3146

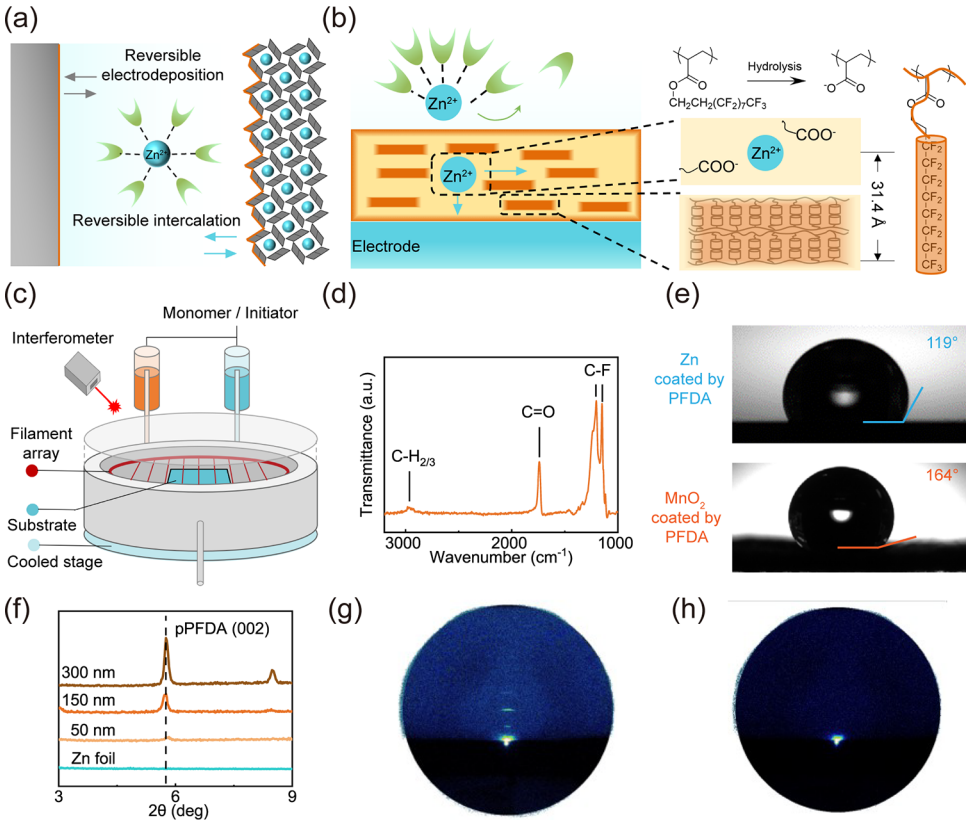

Figure 1. Interphase design, synthesis, and characterization. (a) Schematic illustration of an ideal interphase to facilitate stable and reversible cycling. (b) Schematic illustration of the ultrathin and semicrystalline pPFDA interphases of interest in this study. (c) Illustration of the iCVD setup used to synthesize pPFDA interphases with controlled nanoscale thickness, stoichiometry, and conformality. (d) FTIR spectrum of the as-deposited pPFDA film (thickness = 300 nm). (e) Images of water droplets on pPFDA interphases formed at a planar Zn anode and a porous MnO_2 cathode; the results illustrate that the interphases are poorly wetted by water. (f) XRD analysis of crystalline pPFDA interphases with different thicknesses (in nm) (collected using identical gain); greater crystallinity is achieved in thicker pPFDA films. (g,h) 2D XRD patterns of the pPFDA-coated Zn (g) and uncoated Zn (h), 3−9 degrees.

interferometry with a HeNe laser source (wavelength = 633 nm, JDS Uniphase) was used to monitor the film growth on a Si wafer. The accurate film thickness on the Si wafer substrates was measured postdeposition using a J.A. Woollam spectroscopic ellipsometry at three different incidence angles (65°, 70°, and 75°) using 188 wavelengths from 380 to 900 nm. The data were fit by using a Cauchy-Urbach model.

Preparation of Electrolytes. For electrodeposition and cell performance characterization, $ZnSO_4{\cdot}7H_2O$ was dissolved in DI water to prepare 2 M electrolytes for Zn batteries. 0.5 M $MnSO_4$ was added to 2 M $ZnSO_4$ electrolytes for Zn−MnO_2 full batteries. $CuSO_4{\cdot}5H_2O$ was dissolved in DI water to prepare a 2 M electrolyte for Cu symmetric cells. For the aqueous Li electrolyte solution, 2 M LiTFSI was added to the 94% PEG400 + 6% DI water.

Electrochemical Measurements. Galvanostatic charge/discharge performance of coin cells was tested on Neware battery test systems at room temperature (25 °C ± 1 °C). No climatic or environmental chamber was used. Electrochemical studies were performed using CR2032 coin cells. The area of electrodes in this study is 0.71 cm^2. Symmetric cells were assembled with two 0.25 mm Zn foils and separated by a glass fiber (GF/A, WHA1821047, thickness 0.68 mm, pore size 1 μm). In each coil cell, ∼100 μL of electrolyte was added using a pipet.

In the Zn||MnO_2 coin cell, α-MnO_2 was synthesized via a conventional hydrothermal route, in which a solution that contains 5 mM $KMnO_4$ and 0.3 M HCl was kept at 140 °C for 18 h. All coin cells were assembled under air conditions.

The Zn||MnO_2 pouch cell was constructed with a zinc foil coated with or without PFDA, cathode materials, and separated by a Celgard 3501 membrane as well as a single layer of glass fiber membrane. The cathode materials consist of α-MnO_2 active materials combined with SuperP and PVDA at an 8:1:1 ratio and coated with 3D carbon cloth. The electrode area measures 9 cm^2, while the electrolyte quantity is 300 μL.

Exchange current: cyclic voltammetry was performed using a CHI 600E electrochemical workstation and symmetrical zinc cells in which the glass fiber is used as a separator. Tafel plots of 2 M $ZnSO_4$ aqueous electrolytes were derived from cyclic voltammetry measurements with a scan rate of 200 mV s^{-1}. Exchange current density was calculated from the Tafel plots.

Characterization of Materials. Field-emission scanning electron microscopy (FESEM) was carried out on a Zeiss Gemini 500 scanning electron microscope equipped with a Bruker energy-dispersive X-ray (EDX) spectroscopy detector to study the electrodeposition morphology of Zn. Linear sweep voltammetry was performed by using a CH 600E electrochemical workstation. Impedance measurements of all electrolytes were measured using frequency domain dielectric relaxation measurements in the range 10^7−10^{-1} Hz using a Novocontrol Broadband dielectric spectrometer. ATR-FTIR spectra were obtained using a Thermo Scientific spectrometer.

RESULTS AND DISCUSSION

Interphase Design and Characterization. Our choice of the hydrophobic polymer, poly(PFDA) (pPFDA) (Figure 1a), as the interphase on both electrodes was informed by prior work on the iCVD-synthesized pPFDA, showing that (i) the flexible $-CH_2-CH_2-$ linker and the ester bond that connects the $-(CF_2)_7CH_3$ side chain to the polymer backbone facilitate

https://doi.org/10.1021/jacs.3c10638
J. Am. Chem. Soc. 2024, 146, 3136−3146

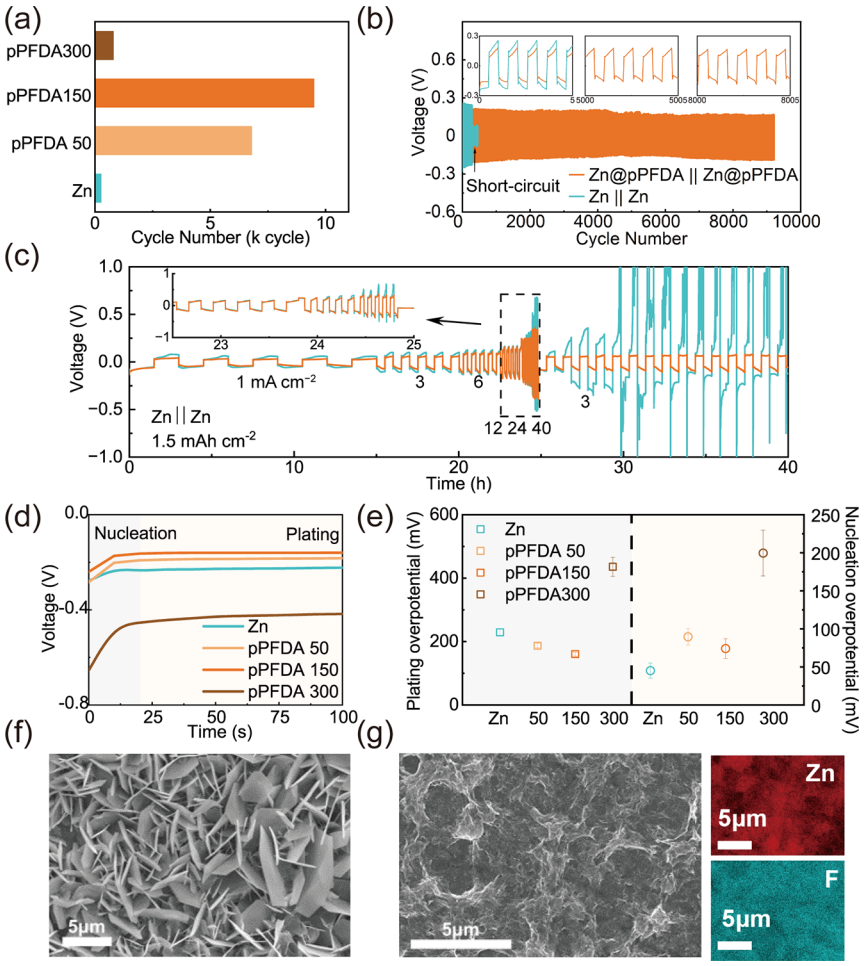

Figure 2. Crystallinity of the pPFDA interphases and the corresponding interfacial stability. (a) Cycle life (in thousands of cycles) achieved in Zn symmetric cells using uncoated Zn (cyan) or Zn coated with varying thicknesses of pPFDA (yellow, orange, and brown); the numbers following the letters "pPFDA" indicate the coating thickness in nm. (b) Plating and stripping cycling voltage profiles of uncoated Zn (cyan) and Zn coated with 150 nm-thick pPFDA (orange); the insets show the detailed voltage profiles for the 0−5, 5000−5005, and 8000−8005 cycles. Data were collected at 40 mA cm^{-2} and a fixed capacity of 1.5 mAh cm^{-2}. (c) Plating and stripping cycling voltage profile or pristine Zn and pPFDA150@Zn under different current densities ranging from 1 to 40 mA cm^{-2} at a areal capacity of 1.5 mAh cm^{-2}. The insets show the detailed voltage profiles for current densities of 12, 24, and 40 mA cm^{-2}. (d) Voltage profiles of single-time plating experiments using uncoated Zn and Zn coated with varying thicknesses of pPFDA. (e) Plating overpotential and nucleation overpotential of uncoated Zn and Zn coated with varying thicknesses of pPFDA. (f) SEM image of a postcycling uncoated Zn electrode, collected after running 100 cycles at 1 mA cm^{-2} and 1 mAh cm^{-2}. (g) SEM image and the corresponding EDX mapping (for Zn and F) of a postcycling Zn electrode coated with 150 nm pPFDA, collected after running 100 cycles at 1 mA cm^{-2} and 1 mAh cm^{-2}.

the self-organization of the fluorinated side chains into an ordered smectic phase;[29] this ordered lamellar structure confers excellent mechanical properties to the ultrathin polymer films, while creating a barrier to water diffusion to the electrode; (ii) the ester bond can be readily hydrolyzed in an aqueous environment,[30] creating $-COO^-$ moieties that serve as ion channels to facilitate the diffusion of metal cations[31] (Figure 1b), promoting large and uniform ion fluxes during battery charging. The introduction of hydrolysis decouples the seemingly conflicting design requirements, integrating three essential functions, i.e., stability, water resistance, and ion conductivity into a single monomer. The crystalline regions in pPFDA reinforce mechanical strength and water resistance, whereas the amorphous regions transform into ion-conducting channels upon cycling due to their susceptibility to hydrolysis.

The pPFDA thin films were synthesized in a single step on the MnO_2 composite cathode and Zn metal anode (kept at 20 °C using a cooled stage) using the all-dry and substrate-independent iCVD technique (Figure 1c). Heterogeneous polymerization occurs under constant flow of the monomer PFDA (at 0.15 sccm) and an initiator, i.e., *tert*-butylperoxide (TBPO, at 0.6 sccm). The initiator to monomer flow rate ratio was kept higher in this case (i.e., 4) than in most iCVD conditions and the stage temperature was kept lower to promote the formation of orientated polymer crystals.[29] Free radicals were generated by homolytic cleavage of TBPO upon flowing through a hot filament array (kept at 300 °C), which impinged on the surface-adsorbed monomer to initiate chain-growth polymerization. Note that this filament temperature is chosen because it leads to the formation of methyl radicals, which cause less distortion of the pPFDA lattice during synthesis and higher film crystallinity (likely due to the small steric hindrance associated with methyl radicals). Furthermore, high filament temperatures are believed to lead to bilayer pPFDA crystals oriented parallel to the substrate surface and

https://doi.org/10.1021/jacs.3c10638
J. Am. Chem. Soc. 2024, 146, 3136−3146

films with enhanced smoothness and conformality, ensuring its conformality on the MnO_2 cathode.[29,32] Under these conditions, we achieved a deposition rate of 35 nm/min, translating to a 5 min preparation time for the conformal pPFDA interphases, starting from the small-molecule precursors. The iCVD technique has also been demonstrated in a roll-to-roll configuration,[33] pointing to scalable semicontinuous manufacturing of these interphases.

The molecular structure of the pPFDA coating was confirmed by Fourier transform infrared (FTIR) spectroscopy (Figure 1d), where the peaks at 3000, 1739, 1203, and 1150 cm^{-1} were attributed to the alkyl, C═O, $-CF_2$, and $-CF_2CF_3$ groups, respectively.[34] Additionally, we used X-ray photoelectron spectroscopy (XPS) to confirm the presence of C, O, and F elements in a survey scan (Figure S2). The pPFDA interphase exhibited strong hydrophobicity, with water contact angles of 119 ± 0.4° and 164 ± 2.1° on the planar Zn anode and MnO_2 composite cathode, respectively (Figure 1e).

The dense packing of the fluorinated side chains (i.e., $-(CF_2)_7CH_3$) in pPFDA is known to drive spontaneous formation of a crystalline smectic B phase.[35] The formation of this phase was confirmed using X-ray diffraction (XRD) (Figure 1f−h) and atomic force microscopy (AFM) (Figure S3). The thickness of the pPFDA coating may also be tuned systematically to optimize the film crystallinity, with the additional goal of balancing the trade-off between the enhanced mechanical properties and reduced ion transport (due to the reduced molecular mobility in the thin film) observed at high crystallinity. Conveniently, the crystallinity of the iCVD-synthesized pPFDA can be controlled precisely by tuning the film thickness, and the film thickness has been used in prior research to predict the size of the crystalline domains in a pPFDA film.[32,36] Thus, we chose three film thicknesses, 50, 150, and 300 nm, denoted as pPFDA50, pPFDA150, and pPFDA300, respectively, to demonstrate the tunable polymer crystallinity and optimize it for interphase stability and transport properties. The thickness was quantified by using spectroscopic ellipsometry (Figure S4). The crystallographic features of these pPFDA films deposited on Zn were illustrated using XRD, which captured the characteristic peak for pPFDA crystals (assigned to (002)) at 5.7° (Figure 1f). The crystallinity underwent a remarkable increase as the film thickness increased from 50 to 300 nm. In addition, pPFDA300 demonstrated a unique peak at 8.5° that was assigned to (003), implying a complete crystallization. As such, we estimated the percentage crystallinity of pPFDA150 and pPFDA50, by taking the ratio of their peak at 5.7° to that of pPFDA300, to be 5.5 and 43.6%, respectively. We further performed 2D XRD (Figure 1g,h) to reveal a narrow full width at half-maximum (fwhm) of the (002) diffraction peak along the χ angle (4°), indicating a preferred crystallographic orientation of the fluorinated side chain that was perpendicular to the Zn metal surface. The crystalline domains are largely impermeable to water diffusion,[37] thus creating a tortuous path for water molecules to reach the electrode surface and inhibiting side reactions like HER. The polymer crystals have also been shown to improve mechanical and chemical stability,[38] which further boosts the interfacial stability at the electrodes. Below, we demonstrate how these oriented crystalline domains in the polymer interphases improve the interfacial stability and, thereby, the performance of aqueous batteries.

Crystallinity and Interfacial Stability. We followed a well-established protocol to evaluate the stability of the pPFDA coatings on Zn using repeated electroplating and stripping in a Zn−Zn symmetric cell under galvanostatic conditions. In these experiments, cells were cycled at a current density of 40 mA/cm^2 and at a capacity of 1.5 mAh/cm^2 to simultaneously ensure rapid interfacial evolution and reasonable volume change for the electrode (i.e., to decrease the chance to damage the polymer film due to large volume changes). As shown in Figure 2a, under these conditions, uncoated Zn electrodes exhibited a limited cycle life of 270 cycles; the cells failed primarily by a shorting mechanism, as evidenced by the sudden voltage drop in Figure 2b. The truncated cycling life is fundamentally attributable to the heterogeneous interphases spontaneously formed at the Zn electrode and the parasitic HER, as discussed above. By comparison, symmetric cells made with pPFDA-coated Zn achieved varying degrees of enhanced stability (Figure 2a). The pPFDA50 coating led to a cycle life of at least 6800 cycles with a potential profile that revealed a sudden voltage change at around 3000 and 3500 cycles (Figure S4). The pPFDA150 coating led to stable plating and stripping cycles, with a cycle number as high as 9500 (Figure 2b), corresponding to a 35-fold enhancement compared to the control group. pPFDA300 led to an increased overpotential and a cycling life of merely 800 cycles (Figure S5). We attributed the varying effects of the pPFDA coatings with different thicknesses to the degree of crystallinity. Specifically, the pPFDA50 coating exhibited a low crystallinity (i.e., 5.5% that of pPFDA300) and thus demonstrated marginal improvements in the cycling life of symmetric cells due to poor mechanical stability, whereas the pPFDA300 coating with high crystallinity inhibited ion transportation and led to high overpotential and nonuniform ion flux. To highlight the advantages of the pPFDA150 coating in enabling stable cycling under a variety of current densities, cells with an areal capacity of 1.5 mAh/cm^2 were cycled at current densities ranging from 1 to 40 mA/cm^2 for 5 cycles (Figure 2c). The uncoated Zn electrodes exhibited high overpotentials, i.e., 60 mV at 1 mA/cm^2 and 95 mV at 3 mA/cm^2. They failed after 25 h, as evidenced by the large overpotential and disordered voltage profiles. In contrast, pPFDA150-coated Zn electrodes demonstrated low overpotentials, i.e., 27 mV at 1 mA/cm^2 and 55 mV at 3 mA/cm^2, with the capability to cycle stably for at least 500 h at a low current density of 2 mA/cm^2 (Figure S7). The electrochemical performance of the ultrathin pPFDA150 coating compares favorably to other polymer coatings reported to date (Table S1), highlighting the crucial role played by its moderate crystallinity and adaptive hydrolysis.

We further evaluated the interphases using a continuous charging protocol, wherein the Zn ions in solution are electrochemically plated on a polished Zn substrate (without or with the pPFDA interphase) at a fixed current density of 40 mA/cm^2. The corresponding potential response was used to extract the plating and nucleation overpotential under conditions identical to those used in the symmetric cell tests described earlier (see Figure 2d,e). Interestingly, with increasing pPFDA coating thickness, the plating overpotential first decreased from 229 mV (for uncoated Zn) to 160 mV (for pPFDA150-coated Zn) and then increased to 436 mV for pPFDA300-coated Zn. By comparison, the nucleation overpotential followed an increasing trend from 45 mV (for uncoated Zn) to 200 mV (for pPFDA300-coated Zn), although the difference between pPFDA50 and pPFDA150

https://doi.org/10.1021/jacs.3c10638
J. Am. Chem. Soc. 2024, 146, 3136−3146

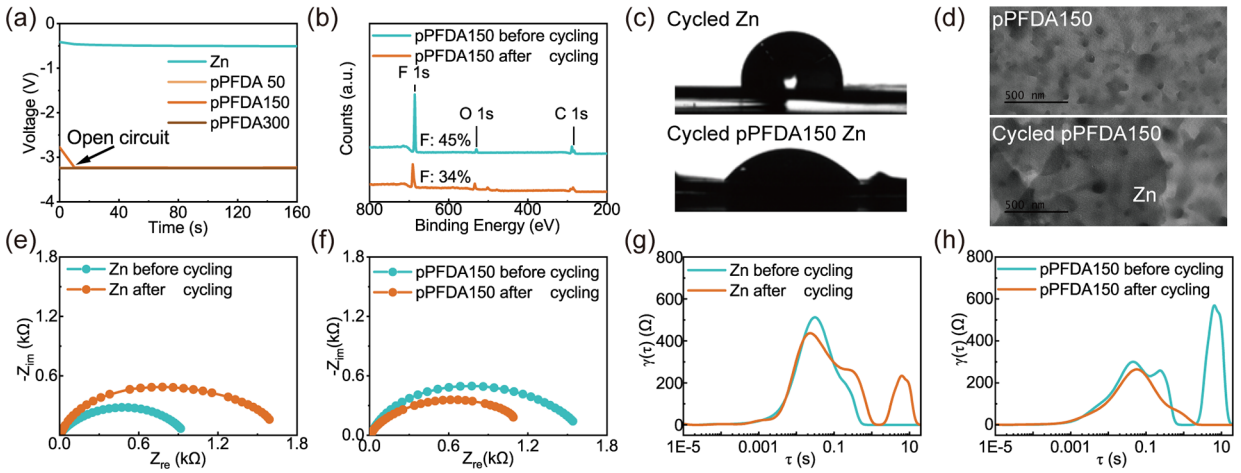

Figure 3. Hydrolysis-enabled formation of the adaptive ion channels. (a) Single-time plating of uncoated Zn and Zn coated with varying thicknesses of pPFDA; plating was performed in a nonaqueous electrolyte comprising 2 M Zn $(TFSI)_2$ in mPEG (M_w = 400 Da). (b) XPS survey scan of the 150 nm pPFDA coating (on Zn) before and after 10 cycles. (c) Images of water droplets on Zn foil electrodes, with and without 150 nm-pPFDA, after 10 charge−discharge cycles. (d) TEM images of uncycled and cycled pPFDA150, indicating the presence and preservation of pores during cycling. (e,f) Nyquist plots of (e) uncoated and (f) pPFDA150-coated Zn symmetric cells before and after cycling. (g,h) DRT transformation of the EIS results in (e,f).

are statistically insignificant (90 mV ± 11 mV for PFDA50 and 74 mV ± 13 mV for PFDA150). We attributed the difference in plating and nucleation overpotential to the overall effects of the reduced parasitic reaction and the increased impedance from the crystalline interphase. Furthermore, the crystalline domains led to added benefits for the electrodeposition of Zn, as discussed below.

The morphology of the Zn electrode was examined using scanning electron microscopy (SEM) after 100 cycles of electroplating and stripping, as shown in Figure 2f,g. The uncoated Zn exhibited a porous network structure composed of numerous hexagonal Zn metal disks oriented nearly parallel to the electrode surface normal vector (Figure 2f); this finding is consistent with the literature[7] and also explains the rather quick battery shorting observed in cycling studies (Figure 2a,b). An examination of the Zn side of the current collector in contact with the Zn electrode showed a rapid accumulation of "orphaned" Zn, which provides an additional explanation for the rapid capacity fading. In contrast, pPFDA150-coated Zn, after 100 cycles of electroplating and stripping, maintained a relatively flat morphology. We further confirmed that the pPFDA coating remained uniform on the Zn surface, as indicated by the evenly distributed F signal obtained using EDX spectroscopy. The contrast between the uncoated and coated Zn electrodes revealed that the pPFDA150 interphase and its moderate crystallinity led to excellent interfacial stability and uniform electrodeposition.

Formation of the Ion Channels. A key discovery from our study is that in aqueous electrolytes, pPFDA undergoes a hydrolysis reaction which produces ion channels that facilitate interfacial ion transport. The facilitated ion transport is the most plausible source of the reduced interfacial impedance observed during cycling of Zn−MnO_2 batteries. As a point of comparison, we prepared a nonaqueous electrolyte, composed of methyl-terminated poly(ethylene glycol) (mPEG) (with 2 M $Zn(TFSI)_2$. Interestingly, irrespective of the thickness of the pPFDA interphases formed in the mPEG electrolyte, interfacial ion transport is always sluggish, as indicated by the occurrence of an open circuit shortly after applying the current (Figure 3a). In contrast, the pPFDA interphases regained considerable ionic conductivity, which led to stable cycling, simply by replacing half of the mPEG solvent with water (Figure S8). We postulate that the hydrolysis of the fluorinated pendent group "activated" the ion channels during battery cycling. To test this hypothesis, we performed an XPS survey scan of the pPFDA-coated Zn electrode after 100 cycles (Figure 3b), which indicated that the atomic ratio of F decreased from 45% (a small deviation from the theoretical value of 53% for pure PFDA due to the presence of adventitious carbon) to 34%, pointing to a hydrolysis reaction conversion of 67.6%. Additionally, we acquired the FTIR spectra of pPFDA-coated Zn before and after long cycling (Figure S9). A peak shift for the C═O group, from 1740 cm^{-1} (assigned to ester) before hydrolysis to 1640 cm^{-1} (assigned to carboxylate) after hydrolysis, indicates the occurrence of hydrolysis during cycling. The occurrence of hydrolysis was further corroborated by water contact angle (WCA) measurements as the hydrolysis reaction converts the fluorinated side chain to a carboxylic acid one and thus increases the hydrophilicity of the synthetic interphase. Indeed, after 100 cycles, the WCA of a pPFDA150-coated Zn anode decreased from 118° to 44°, whereas the WCA of an uncoated Zn anode increased from 91° to 101°, the latter corresponding to zinc oxide (Figures S10 and 3c).[39] Interestingly, the moderate crystallinity in pPFDA150 also contributed to a slower hydrolysis rate as pPFDA50 demonstrated a WCA of 28° after 100 cycles. Therefore, we argue that the conversion of the fluorinated side chains to carboxylic acid ones occurred more rapidly in the amorphous phase of the synthetic interphase, enhancing the wetting of the interface without sacrificing the reduced water permeability entirely.[40] We confirmed preferential hydrolysis by demonstrating that cycling did not change the crystallinity of the pPFDA150 interphase using XRD (Figure S11). The heterogeneity of pPFDA150 is preserved before and after the cycling, as shown in the transmission electron microscopy (TEM) images in Figure 3d. As such, we postulate that the controlled moderate crystallinity of pPFDA150 was critical to achieving the balance between interfacial stability and ion transport in aqueous batteries. Interestingly, the hydrolyzed film remains effective at protecting the Zn anode from side

https://doi.org/10.1021/jacs.3c10638
J. Am. Chem. Soc. 2024, 146, 3136−3146

reactions, as demonstrated in the XRD spectra of the Zn anodes with and without the coating after 40 h of cycling (Figure S12). While pristine Zn showed significant ZnO peaks after cycling, no detectable peaks were identified on the pPFDA150-coated Zn, indicating the coating's protective capability throughout hydrolysis. We attributed this protection effect to the high crystallinity of pPFDA and the incomplete hydrolysis in the amorphous region during cycling. The hydrophobic crystalline regions slow the diffusion of water molecules through the coating, and the remaining hydrophobic moieties prevent water from penetrating and reacting with Zn.

To further understand the transport behavior of charged species through the pPFDA interphase, we performed electrochemical impedance spectroscopy (EIS) measurements in an aqueous electrolyte. Uncoated Zn yields a Nyquist plot with gradually expanding semicircles, indicating the continuous occurrence of parasitic reactions in the interphase. The interfacial impedance increased from 961 Ohms (before cycling) to 1773 Ohms after 100 cycles (Figure 3e). Unsurprisingly, the interfacial impedance decreased for the pPFDA150 interphase from 1425 to 962 Ohms after 100 cycles, corroborating the reduced resistance as a result of the hydrolysis reaction. This reduced interfacial impedance represented the overall outcome of the competing factors of (i) hydrolysis of the pPFDA thin film and (ii) formation of a passivation layer from side reactions, thus indicating that the formation of ion channels dominated the evolution of the charge transfer (Figure 3f).

The distribution of relaxation times (DRT) methodology provides additional insights about interfacial ion transport phenomena by transforming the frequency domain-based Nyquist plots into time domain-based DRT spectra. We chose the DRT analysis (e.g., rather than equivalent circuit fits) because it does not require prior knowledge of the system, while distinguishing the specific electrochemical processes without the need for simulation, as reported previously.[41] Our analysis reveals three major peaks at around $\tau = 10^{-3}$–10^{-1} s, 10^{-1}–1 s, and 10 s point to three distinct electrochemical processes on the Zn anode (Figure 3g,h), two of which (at $\tau = 10^{-3}$–10^{-1} s and 10^{-1}–1) remained after 100 cycles that were attributed to the charge transfer of water and zinc ions on the surface. While more detailed experiments were required to fully designate the third peak, it is noteworthy that with the passivation of the Zn interface, new charge transfer processes with a characteristic time of 10 s appeared, representing ion transport at the passivated interphase. In contrast, PFDA150 showed a rather large peak at around $\tau = 10$ s before activation, revealing a sluggish ion transport process. After cycling, the peak at $\tau = 10$ s disappeared, which is attributed to the rapid ion transport between the carboxyl groups formed by the hydrolysis of PFDA.

We estimated the Zn transference number from potentiostatic polarization and Nyquist plot measurements before and after polarization, which played a critical role in electrode overpotential and cycling stability. The results reported in Figure 4b indicate that the Zn transference number with pPFDA150 is approximately 0.76, which is noticeably higher than that estimated for the uncoated Zn, i.e., 0.26. This finding is consistent with a previous report which shows that ion-selective Nafion coatings on Li also dramatically improves the cation transference number.[42] As in that study, we attributed the high transference number to the anionic carboxyl groups, which facilitated cation conduction and hindered anion migration. indicating that the activated pPFDA150 effectively and selectively transported cations through the interphase.

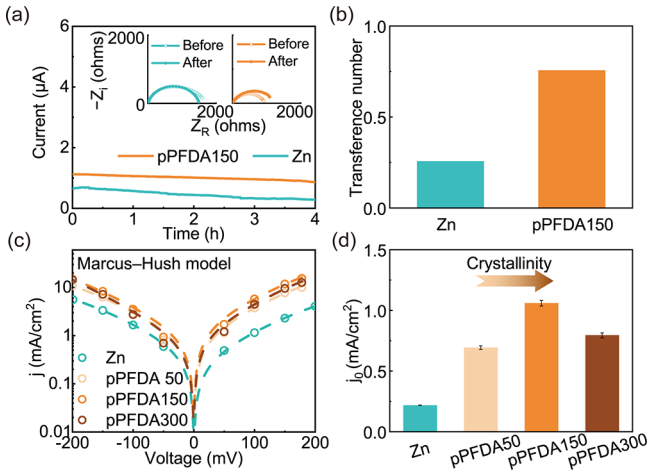

Figure 4. Electrochemical properties of the pPFDA interphase. (a) Chronoamperometric response following a 10 mV step of Zn symmetric cells equipped with pristine Zn or PFDA150-coated Zn. Insets: Nyquist plots of the interfacial properties of the symmetric cells before and after polarization. (b) Zn transference numbers estimated from the data in (a) assuming dilute solution behavior and the Bruce-Vincent analytical method holds. (c) Tafel plots of pristine Zn and PFDA-coated Zn with different thicknesses in 2 M $ZnSO_4$ aqueous solution derived from cyclic voltammetry measurements, fitted by the Marcus–Hush model. (d) Exchange current density of pristine Zn and PFDA-coated Zn with a different thickness derived from (c).

The exchange current density (j_0) was also investigated (Figure 4c,d and Table S2) to understand the impact of the pPFDA interphases on electrochemical reaction kinetics using the Marcus–Hush model.[43] The exchange current density of uncoated Zn was computed to be 0.22 mA/cm^2, approximately 20% of that of pPFDA150-coated Zn (1.06 mA/cm^2). This was attributed to less inert component formation at the interface, leading to efficient mass transport, thus accelerating the deposition/dissolution kinetics. Notably, the reorganization energy of the solvent in response to the initial and final reaction states, i.e., λ, is ~0.41 eV for pristine Zn and 0.43 eV for pPFDA-coated Zn, hinting at the formation of a carboxyl-rich environment in the pPFDA interphase with stronger binding strength to Zn^{2+} than water. Interestingly, pPFDA150 exhibited a higher j_0 than that of pPFDA50 (0.69 mA/cm^2) and pPFDA300 (0.79 mA/cm^2). We attributed the former to a greater amount of orientated crystalline domains in pPFDA150 than pPFDA50, thus greater protection of the Zn surface, and the latter to slow ion transport in a highly crystalline film like pPFDA300.

Full-Cell Performance with Conformal Interphases at Both Electrodes. The iCVD methodology is versatile and can be used to create conformal pPFDA150 coatings on a MnO_2 composite cathode in a single step. SEM images of the coated and uncoated composite cathodes (Figure S13) reveal the characteristic needle-like α-MnO_2 particles, indicating excellent conformity of the pPFDA150 coating. The width of the MnO_2 crystals increased slightly from 114 ± 28 to 169 ± 33 nm after the iCVD process, indicating the presence of the pPFDA coating. The MnO_2 composite cathode also maintained its characteristic crystallographic features, as shown by the unchanged XRD patterns (Figure S14) after iCVD. Building

https://doi.org/10.1021/jacs.3c10638
J. Am. Chem. Soc. 2024, 146, 3136–3146

upon that confirmation, we assembled Zn−MnO_2 full batteries to assess the effect of the pPFDA interphase on cycling stability, with a mass loading of the MnO_2 cathode of 4 mg/cm^2 and the cycling condition of 2 A g^{-1} (8 mA/cm^2). The layered material of α-MnO_2 is known to suffer from severe and irreversible side reactions with an aqueous electrolyte during repeated intercalation/deintercalation, leading to electrochemical instability and rapid capacity loss.[7] Indeed, 20% of the initial capacity of a Zn||MnO_2 cell was lost after merely 35 cycles using uncoated electrodes (Figure 5a) despite the mild

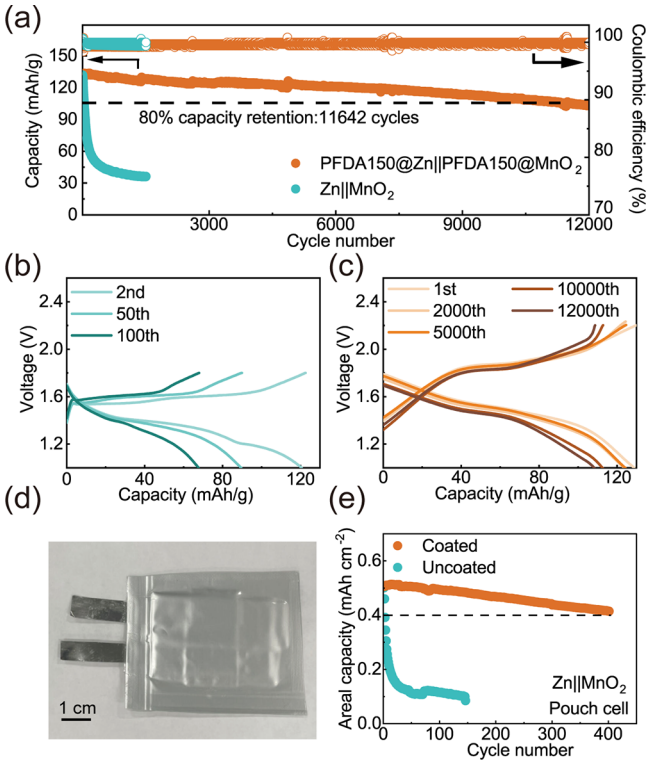

Figure 5. Highly stable Zn-ion aqueous batteries enabled by the pPFDA150 interphase. (a) Discharge capacity and Coulombic efficiency of Zn||MnO_2 cells with and without the PFDA150 coatings. An aqueous electrolyte comprising 2 M $ZnSO_4$ and 0.5 M $MnSO_4$ was used for these studies. (b,c) Voltage−capacity curves for the Zn−MnO_2 full batteries using (b) uncoated Zn and MnO_2 and (c) pPFDA150-coated Zn and pPFDA150-coated MnO_2. The coin cells were cycled at 2 A/g. (d) Photo of a fully assembled pouch cell used in the cycling stability tests in (e). (e) Discharge capacity of Zn||MnO_2 pouch cells using pPFDA-coated or pristine electrodes in an aqueous electrolyte containing 2 M $ZnSO_4$ and 0.5 M $MnSO_4$. The pouch cells were cycled at a current density of 1 mA cm^{-2}.

condition with a cycling window between 1.8 and 1.0 V that was chosen to suppress the irreversible reactions. After 100 cycles, the needle-like morphology evolved into chunky deposits (Figure S15). Additionally, the voltage plateau near 1.2 V disappeared on the charge and discharge curves, and a significant increase in the overpotential was observed (Figure 5b), indicating irreversible damages to the α-MnO_2 structure due to the side reactions and byproducts that blocked the ion transport.

The pPFDA150 interphases on both electrodes improved the cycling stability considerably. Here, we used relatively harsh cycling conditions to make full use of the potential capacity of MnO_2 (i.e., 2.2−1.0 V). After 10 precycles to activate the pPFDA150 ion channels, the battery delivered a cycle life of 11,642 cycles with 80% capacity retention (Figure 5a). The cathode maintained the needle-like morphology after 2000 cycles (Figure S15). Moreover, the battery showed stable performance at different charging/discharging rates ranging from 2 to 10 mA cm^{-2} (Figure S16). This improvement in cycling stability was a direct result of the pPFDA150 interphase and formation of ion channels. The selective permeability of the ion channels could also inhibit the irreversible side reactions between α-MnO_2 and the aqueous electrolyte by promoting reversible cation insertion reactions, as indicated by the higher charge/discharge plateau compared to uncoated Zn||MnO_2 batteries (Figure 5c).

In Zn||MnO_2 batteries, both electrodes are susceptible to degradation by the aqueous electrolyte, rendering the protective coating imperative for both electrodes for stable cycling and an extended cycle life. To illustrate this point, we constructed full batteries, pairing pPFDA-coated Zn with uncoated MnO_2 or pPFDA150-coated MnO_2 with uncoated Zn, and assessed their cycling performance (Figure S17). For the Zn|| pPFDA150@MnO_2 battery, the areal capacity decreased in the first 40 cycles, steadily increased during cycles 40−350, and decreased again beyond cycle 350 until its failure at 1670 cycles. This trend aligns well with the prior reports on MnO_2 batteries, characterized by the competition among electrode reactions involving H^+/Zn^{2+} insertion, Mn^{2+} conversion, and accumulation of inert Zn/Mn species. Water molecules contribute to the dissolution of Mn from the cathode and the formation of inert Zn−Mn species, as extensively discussed in the article by Yang et al.[44] Despite a robust anode, the battery ultimately failed due to cathode issues. In contrast, the pPFDA150@Zn||MnO_2 configuration maintained a consistently high and stable areal capacity at 135 mAh/cm^2, attributing to the protective influence of the pPFDA coating to reduce Mn dissolution. However, this battery experienced a rapid failure at 59 cycles due to Zn dendrite formation, leading to a short circuit. Consequently, addressing challenges related to Mn leaching from the cathode, along with ensuring a stable electrochemical interface, is crucial for achieving stability and a prolonged lifespan in aqueous batteries.

The effectiveness of the pPFDA coating and interphase design strategy is evident through the tangible performance enhancement observed in pouch cells. Pouch cells were constructed using 3 × 3 cm electrodes (Figure 5d) and subject to cycling at 1 mA/cm^2 in an aqueous electrolyte containing 2 M $ZnSO_4$ and 0.5 M $MnSO_4$. Remarkably, the pouch cell with pPFDA-coated electrodes demonstrated stable cycling for an extended duration, reaching 400 cycles (Figure 5e). In stark contrast, the pouch cell utilizing uncoated electrodes exhibited rapid failure after a mere 3 cycles. This substantial and practical improvement in the performance of pouch cells unequivocally underscores the effectiveness and practicality of the pPFDA coating.

Generalization of the pPFDA Interphase Design in Other Aqueous Electrolytes. The interphase design concept is, in principle, applicable to other electrodes that are sensitive to water-related side reactions. We studied its effectiveness in regulating the morphology of electrodeposited Cu and Li. Li and Cu are similar to Zn in that the electrochemical reaction on the electrodes is based on the plating/stripping of solvated metal ions, albeit Li deposits at a substantially more reducing electrode potential, making the electrode intrinsically unstable

https://doi.org/10.1021/jacs.3c10638
J. Am. Chem. Soc. 2024, 146, 3136−3146

in an aqueous electrolyte. While the overpotential of uncoated Cu had a sudden increase after 15 cycles to 0.25 V (Figure S18, left), the pPFDA150 greatly improved the stability with an overpotential of ∼0.2 V under the current density of 40 mA cm^{-2} and an areal capacity of 1.2 mAh cm^{-2}. In order to suppress the reaction between Li and water, an electrolyte of 96% mPEG, 4% water (volume percentage), and 1 M LiTFSI was used. The pristine Li failed to cycle, whereas pPFDA150 enabled reversible plating and stripping of Li at 0.2 mA/cm^2 and 0.05 mAh/cm^2. Nevertheless, the continuously increasing overpotential points to side reactions between Li and water (Figure S18, right). Although not a focus of this paper, further optimization is required to achieve adequate protection of a Li metal anode. In summary, the iCVD-enabled synthesis of pPFDA interphases is broadly applicable to other electrodes, which led to improved stability in an aqueous environment. The coating could improve other aqueous Zn batteries, including Zn−I_2, Zn−S, Zn−V_2O_5, and Zn−air batteries. The design strategies of moderate crystallinity and formation of ion channels will also guide the design of next-generation advanced interphases for metal and composite electrodes in aqueous electrolytes, e.g., aqueous aluminum and lithium batteries.

CONCLUSIONS

In this letter, we demonstrated iCVD as a generalizable synthesis method to create conformal polymer interphases for highly stable next-generation aqueous batteries. In iCVD, polymer synthesis and coating application occur in a single step and in a single chamber, thus incurring minimal operational costs. The iCVD technology has been scaled up to enable semicontinuous manufacturing in a roll-to-roll fashion (by Karaman and co-workers[33] and Cheng and Gupta[45]), which is compatible with the flexible Zn anode and MnO_2 cathode materials. We designed a series of pPFDA interphases with varying crystallinity and unraveled their effects on the interfacial stability and electrochemical properties of the electrodes using Zn−MnO_2 aqueous batteries as an example. By controlling the film thickness deposited on the electrode, the crystallinity could be fine-tuned from an amorphous to a highly crystalline film. The cell cycling performance revealed that moderate crystallinity with orientated polymer crystals achieved an outstanding balance between the film stability and the ion transport properties. The symmetric cell delivered a stable cycling over 9500 cycles, which is 35 times larger than the uncoated group of 270 cycles.

Interestingly, the fluorinated side chains in the amorphous domain of the pPFDA interphases are readily hydrolyzed to form cation transport channels made of carboxyl groups. The carboxyl-rich environment facilitated the desolvation of Zn^{2+}, increasing the transference number to 0.76 (from 0.26 for uncoated Zn) and the exchange current density to 1.01 mA/cm^{-2} (from 0.35 mA/cm^{-2} for uncoated Zn). Beyond the anode, pPFDA150 was proven to protect the MnO_2 particles on the cathode from irreversible side reactions. Using pPFDA150 on both electrodes, the cycle life of a Zn-MnO_2 battery was prolonged from 35 to over 11,000 cycles. The method and the specific interphase design were extended to Cu and Li anodes that faced challenges similar to those of Zn in aqueous electrolytes. The spontaneous hydrolysis potentially delivers protection of the metal anodes by the inert fluorinated coating during storage and autonomous activation upon battery cycling. To further exploit hydrolysis to create even better-tailored coatings, future work will focus on multifunctional copolymers or thin films with gradient compositions, which bear side groups with varying degrees of susceptibility to hydrolysis to fine-tune the film stability, water activity, and ion conductivity of the coating. The universality of the approach to create a conformal interphase and the design principle for the polymer interphase in aqueous electrolyte inform the design and optimization of other aqueous electrochemical systems by enabling a stable interface, paving the way to next-generation cost-effective energy storage systems.

ASSOCIATED CONTENT

Supporting Information

The Supporting Information is available free of charge at https://pubs.acs.org/doi/10.1021/jacs.3c10638.

Additional benchmarking of cycling performance, material characterization, and electrochemical analysis (PDF)

AUTHOR INFORMATION

Corresponding Authors

Lynden A. Archer − *School of Chemical and Biomolecular Engineering, Cornell University, Ithaca, New York 14853, United States;* orcid.org/0000-0001-9032-2772; Email: laa25@cornell.edu

Rong Yang − *School of Chemical and Biomolecular Engineering, Cornell University, Ithaca, New York 14853, United States;* orcid.org/0000-0001-6427-026X; Email: ryang@cornell.edu

Authors

Pengyu Chen − *School of Chemical and Biomolecular Engineering, Cornell University, Ithaca, New York 14853, United States;* orcid.org/0000-0002-0420-8576

Shuo Jin − *School of Chemical and Biomolecular Engineering, Cornell University, Ithaca, New York 14853, United States;* orcid.org/0000-0003-0425-9143

Shifeng Hong − *Materials Science and Engineering, Bard Hall, Cornell University, Ithaca, New York 14853, United States*

Yufeng Qiu − *School of Chemical and Biomolecular Engineering, Cornell University, Ithaca, New York 14853, United States*

Zheyuan Zhang − *School of Chemical and Biomolecular Engineering, Cornell University, Ithaca, New York 14853, United States*

Yuanze Xu − *School of Chemical and Biomolecular Engineering, Cornell University, Ithaca, New York 14853, United States;* orcid.org/0000-0002-4873-6629

Yong Lak Joo − *School of Chemical and Biomolecular Engineering, Cornell University, Ithaca, New York 14853, United States;* orcid.org/0000-0002-4646-1625

Complete contact information is available at: https://pubs.acs.org/10.1021/jacs.3c10638

Author Contributions

[§]P.C. and S.J. contributed equally.

Notes

The authors declare no competing financial interest.

ACKNOWLEDGMENTS

The project is sponsored by the Department of the Navy, Office of Naval Research under ONR Award N00014-20-1-

2418, awarded to R.Y. Additionally, we extend our gratitude to the Center for Mesoscale Transport Properties, an Energy Frontier Research Center supported by the U.S. Department of Energy, Office of Science, Basic Energy Sciences, under award #DE-SC0012673. We also wish to express our appreciation for the Samuel C. Fleming Family Graduate Fellowship and KIC Graduate Fellowship at Cornell University for the support granted to P.C. Furthermore, we acknowledge the valuable resources and facilities made available through the Cornell Center for Materials Research (CCMR), funded by the NSF MRSEC program (DMR-1719875).

REFERENCES

(1) Zhao, C.-X.; Liu, J.-N.; Wang, J.; Wang, C.; Guo, X.; Li, X.-Y.; Chen, X.; Song, L.; Li, B.-Q.; Zhang, Q. A clicking confinement strategy to fabricate transition metal single-atom sites for bifunctional oxygen electrocatalysis. *Sci. Adv.* **2022**, *8* (11), No. eabn5091.

(2) Zheng, J.; Deng, Y.; Yin, J.; Tang, T.; Garcia-Mendez, R.; Zhao, Q.; Archer, L. A. Textured Electrodes: Manipulating Built-In Crystallographic Heterogeneity of Metal Electrodes via Severe Plastic Deformation. *Adv. Mater.* **2022**, *34* (1), No. 2106867.

(3) Spoerke, E. D.; Passell, H.; Cowles, G.; Lambert, T. N.; Yadav, G. G.; Huang, J.; Banerjee, S.; Chalamala, B. Driving Zn-MnO2 grid-scale batteries: A roadmap to cost-effective energy storage. *MRS Energy & Sustainability* **2022**, *9* (1), 13−18.

(4) Yu, P.; Zeng, Y.; Zhang, H.; Yu, M.; Tong, Y.; Lu, X. Flexible Zn-Ion Batteries: Recent Progresses and Challenges. *Small* **2019**, *15* (7), No. 1804760.

(5) Aubin, C. A.; Choudhury, S.; Jerch, R.; Archer, L. A.; Pikul, J. H.; Shepherd, R. F. Electrolytic vascular systems for energy-dense robots. *Nature* **2019**, *571* (7763), 51−57.

(6) Chao, D.; Zhou, W.; Xie, F.; Ye, C.; Li, H.; Jaroniec, M.; Qiao, S.-Z. Roadmap for advanced aqueous batteries: From design of materials to applications. *Sci. Adv.* **2020**, *6* (21), No. eaba4098.

(7) Jin, S.; Yin, J.; Gao, X.; Sharma, A.; Chen, P.; Hong, S.; Zhao, Q.; Zheng, J.; Deng, Y.; Joo, Y. L.; Archer, L. A. Production of fast-charge Zn-based aqueous batteries via interfacial adsorption of ion-oligomer complexes. *Nat. Commun.* **2022**, *13* (1), 2283.

(8) Fang, G.; Zhou, J.; Pan, A.; Liang, S. Recent Advances in Aqueous Zinc-Ion Batteries. *ACS Energy Lett.* **2018**, *3* (10), 2480−2501.

(9) Cao, L.; Li, D.; Pollard, T.; Deng, T.; Zhang, B.; Yang, C.; Chen, L.; Vatamanu, J.; Hu, E.; Hourwitz, M. J.; Ma, L.; Ding, M.; Li, Q.; Hou, S.; Gaskell, K.; Fourkas, J. T.; Yang, X.-Q.; Xu, K.; Borodin, O.; Wang, C. Fluorinated interphase enables reversible aqueous zinc battery chemistries. *Nat. Nanotechnol.* **2021**, *16* (8), 902−910.

(10) Naveed, A.; Rasheed, T.; Raza, B.; Chen, J.; Yang, J.; Yanna, N.; Wang, J. Addressing thermodynamic Instability of Zn anode: classical and recent advancements. *Energy Storage Mater.* **2022**, *44*, 206−230.

(11) Guo, X.; Zhou, J.; Bai, C.; Li, X.; Fang, G.; Liang, S. Zn/MnO2 battery chemistry with dissolution-deposition mechanism. *Mater. Today Energy* **2020**, *16*, No. 100396.

(12) Li, Y.; Wang, S.; Salvador, J. R.; Wu, J.; Liu, B.; Yang, W.; Yang, J.; Zhang, W.; Liu, J.; Yang, J. Reaction Mechanisms for Long-Life Rechargeable Zn/MnO2 Batteries. *Chem. Mater.* **2019**, *31* (6), 2036−2047.

(13) Wang, Z.; Zhou, M.; Qin, L.; Chen, M.; Chen, Z.; Guo, S.; Wang, L.; Fang, G.; Liang, S. Simultaneous regulation of cations and anions in an electrolyte for high-capacity, high-stability aqueous zinc−vanadium batteries. *eScience* **2022**, *2* (2), 209−218.

(14) Zou, Y.; Liu, T.; Du, Q.; Li, Y.; Yi, H.; Zhou, X.; Li, Z.; Gao, L.; Zhang, L.; Liang, X. A four-electron Zn-I2 aqueous battery enabled by reversible I−/I2/I+ conversion. *Nat. Commun.* **2021**, *12* (1), 170.

(15) Cao, L.; Li, D.; Hu, E.; Xu, J.; Deng, T.; Ma, L.; Wang, Y.; Yang, X.-Q.; Wang, C. Solvation Structure Design for Aqueous Zn Metal Batteries. *J. Am. Chem. Soc.* **2020**, *142* (51), 21404−21409.

(16) Zhao, K.; Fan, G.; Liu, J.; Liu, F.; Li, J.; Zhou, X.; Ni, Y.; Yu, M.; Zhang, Y.-M.; Su, H.; Liu, Q.; Cheng, F. Boosting the Kinetics and Stability of Zn Anodes in Aqueous Electrolytes with Supramolecular Cyclodextrin Additives. *J. Am. Chem. Soc.* **2022**, *144* (25), 11129−11137.

(17) Blanc, L. E.; Kundu, D.; Nazar, L. F. Scientific Challenges for the Implementation of Zn-Ion Batteries. *Joule* **2020**, *4* (4), 771−799.

(18) Kundu, D.; Hosseini Vajargah, S.; Wan, L.; Adams, B.; Prendergast, D.; Nazar, L. F. Aqueous vs. nonaqueous Zn-ion batteries: consequences of the desolvation penalty at the interface. *Energy Environ. Sci.* **2018**, *11* (4), 881−892.

(19) Cao, L.; Li, D.; Deng, T.; Li, Q.; Wang, C. Hydrophobic Organic-Electrolyte-Protected Zinc Anodes for Aqueous Zinc Batteries. *Angew. Chem., Int. Ed.* **2020**, *59* (43), 19292−19296.

(20) Wu, M.; Zhang, G.; Yang, H.; Liu, X.; Dubois, M.; Gauthier, M. A.; Sun, S. Aqueous Zn-based rechargeable batteries: Recent progress and future perspectives. *InfoMat* **2022**, *4* (5), No. e12265.

(21) Chen, R.; Liu, Q.; Xu, L.; Zuo, X.; Liu, F.; Zhang, J.; Zhou, X.; Mai, L. Zwitterionic Bifunctional Layer for Reversible Zn Anode. *ACS Energy Lett.* **2022**, *7* (5), 1719−1727.

(22) Cai, Z.; Ou, Y.; Zhang, B.; Wang, J.; Fu, L.; Wan, M.; Li, G.; Wang, W.; Wang, L.; Jiang, J.; Seh, Z. W.; Hu, E.; Yang, X.-Q.; Cui, Y.; Sun, Y. A Replacement Reaction Enabled Interdigitated Metal/Solid Electrolyte Architecture for Battery Cycling at 20 mA cm−2 and 20 mAh cm−2. *J. Am. Chem. Soc.* **2021**, *143* (8), 3143−3152.

(23) Qiu, M.; Jia, H.; Lan, C.; Liu, H.; Fu, S. An enhanced kinetics and ultra-stable zinc electrode by functionalized boron nitride intermediate layer engineering. *Energy Storage Mater.* **2022**, *45*, 1175−1182.

(24) Zhu, M.; Hu, J.; Lu, Q.; Dong, H.; Karnaushenko, D. D.; Becker, C.; Karnaushenko, D.; Li, Y.; Tang, H.; Qu, Z.; Ge, J.; Schmidt, O. G. A Patternable and In Situ Formed Polymeric Zinc Blanket for a Reversible Zinc Anode in a Skin-Mountable Microbattery. *Adv. Mater.* **2021**, *33* (8), No. 2007497.

(25) Khlyustova, A.; Cheng, Y.; Yang, R. Vapor-deposited functional polymer thin films in biological applications. *J. Mater. Chem. B* **2020**, *8* (31), 6588−6609.

(26) Cheng, Y.; Khlyustova, A.; Chen, P.; Yang, R. Kinetics of All-Dry Free Radical Polymerization under Nanoconfinement. *Macromolecules* **2020**, *53*, 10699 DOI: 10.1021/acs.macromol.0c01534.

(27) Stalin, S.; Chen, P.; Li, G.; Deng, Y.; Rouse, Z.; Cheng, Y.; Zhang, Z.; Biswal, P.; Jin, S.; Baker, S. P.; Yang, R.; Archer, L. A. Ultrathin zwitterionic polymeric interphases for stable lithium metal anodes. *Matter* **2021**, *4* (11), 3753−3773.

(28) Chen, S.; Nian, Q.; Zheng, L.; Xiong, B.-Q.; Wang, Z.; Shen, Y.; Ren, X. Highly reversible aqueous zinc metal batteries enabled by fluorinated interphases in localized high concentration electrolytes. *J. Mater. Chem. A* **2021**, *9* (39), 22347−22352.

(29) Perrotta, A.; Christian, P.; Jones, A. O. F.; Muralter, F.; Coclite, A. M. Growth Regimes of Poly(perfluorodecyl acrylate) Thin Films by Initiated Chemical Vapor Deposition. *Macromolecules* **2018**, *51* (15), 5694−5703.

(30) Shindler, S.; Yang, R. Hydrolysis of Poly(fluoroacrylate) Thin Films Synthesized from the Vapor Phase. *Langmuir* **2023**, *39* (3), 1215−1226.

(31) You, J. B.; Yoo, Y.; Oh, M. S.; Im, S. G. Simple and Reliable Method to Incorporate the Janus Property onto Arbitrary Porous Substrates. *ACS Appl. Mater. Interfaces* **2014**, *6* (6), 4005−4010.

(32) Coclite, A. M.; Shi, Y.; Gleason, K. K. Controlling the Degree of Crystallinity and Preferred Crystallographic Orientation in Poly-Perfluorodecylacrylate Thin Films by Initiated Chemical Vapor Deposition. *Adv. Funct. Mater.* **2012**, *22* (10), 2167−2176.

(33) Şakalak, H.; Yilmaz, K.; Gürsoy, M.; Karaman, M. Roll-to-Roll Vapor Deposition of Hydrophobic and Transparent Nano-Adhesive Polymeric Thin Films on Rigid and Flexible Substrates. *Ind. Eng. Chem. Res.* **2022**, *61* (25), 8839−8846.

(34) Bayram, F.; Mercan, E. S.; Karaman, M. One-step fabrication of superhydrophobic-superoleophilic membrane by initiated chemical vapor deposition method for oil−water separation. *Colloid Polym. Sci.* **2021**, *299* (9), 1469−1477.

(35) Honda, K.; Morita, M.; Otsuka, H.; Takahara, A. Molecular Aggregation Structure and Surface Properties of Poly(fluoroalkyl acrylate) Thin Films. *Macromolecules* **2005**, *38* (13), 5699−5705.
(36) Xia, F.; Razavi, B.; Xu, H.; Cheng, Z. Y.; Zhang, Q. M. Dependence of threshold thickness of crystallization and film morphology on film processing conditions in poly(vinylidene fluoride−trifluoroethylene) copolymer thin films. *J. Appl. Phys.* **2002**, *92* (6), 3111−3115.
(37) Pokorny, R.; Seda, L.; Grof, Z.; Hajova, H.; Kosek, J., Diffusion in semi-crystalline polymers. In *Comput.-Aided Chem. Eng.*; Jeżowski, J.; Thullie, J., Eds.; Elsevier: 2009; Vol. *26*, pp 961−966.
(38) Zhang, M. C.; Guo, B.-H.; Xu, J. A Review on Polymer Crystallization Theories. *Crystals* **2017**, *7* (1), 4.
(39) Dave, P. Y.; Patel, K. H.; Chauhan, K. V.; Chawla, A. K.; Rawal, S. K. Examination of Zinc Oxide Films Prepared by Magnetron Sputtering. *Procedia Technol.* **2016**, *23*, 328−335.
(40) Park, S. H.; Byeon, S. Y.; Park, J.-H.; Kim, C. Insight into the Critical Role of Surface Hydrophilicity for Dendrite-Free Zinc Metal Anodes. *ACS Energy Lett.* **2021**, *6* (9), 3078−3085.
(41) Lu, Y.; Zhao, C.-Z.; Zhang, R.; Yuan, H.; Hou, L.-P.; Fu, Z.-H.; Chen, X.; Huang, J.-Q.; Zhang, Q. The carrier transition from Li atoms to Li vacancies in solid-state lithium alloy anodes. *Sci. Adv.* **2021**, *7* (38), No. eabi5520.
(42) Tu, Z.; Choudhury, S.; Zachman, M. J.; Wei, S.; Zhang, K.; Kourkoutis, L. F.; Archer, L. A. Designing Artificial Solid-Electrolyte Interphases for Single-Ion and High-Efficiency Transport in Batteries. *Joule* **2017**, *1* (2), 394−406.
(43) Boyle, D. T.; Kong, X.; Pei, A.; Rudnicki, P. E.; Shi, F.; Huang, W.; Bao, Z.; Qin, J.; Cui, Y. Transient Voltammetry with Ultramicroelectrodes Reveals the Electron Transfer Kinetics of Lithium Metal Anodes. *ACS Energy Lett.* **2020**, *5* (3), 701−709.
(44) Yang, H.; Zhou, W.; Chen, D.; Liu, J.; Yuan, Z.; Lu, M.; Shen, L.; Shulga, V.; Han, W.; Chao, D. The origin of capacity fluctuation and rescue of dead Mn-based Zn−ion batteries: a Mn-based competitive capacity evolution protocol. *Energy Environ. Sci.* **2022**, *15* (3), 1106−1118.
(45) Cheng, C.; Gupta, M. Roll-to-Roll Surface Modification of Cellulose Paper via Initiated Chemical Vapor Deposition. *Ind. Eng. Chem. Res.* **2018**, *57* (34), 11675−11680.

NOTE ADDED AFTER ASAP PUBLICATION

The abstract graphic was corrected on February 7, 2024.

https://doi.org/10.1021/jacs.3c10638
J. Am. Chem. Soc. 2024, 146, 3136−3146